Plasma heating by electron cyclotron wave and the temperature effects on lower hybrid current drive on EAST

M.H. Li [a], H.D. Xu [a]*, X.J. Wang [a], M. Wang [a], B.J. Ding [a]*, C.B. Wu [a], G.H. Yan [a, b], L. Liu [a], L.M. Zhao [a], Z.G. Wu [a], W.Y. Xu [a], D.J. Wu [a], L.Y. Zhang [a], Y.Y. Tang [a], H. Li [c], G.M. Wallace [d], S.G. Baek [d], P.T. Bonoli [d], Q. Zang [a], S.Y. Lin [a], L.Y. Meng [a], H.L. Zhao [a], L.Q. Xu [a], M.R. Wang [a], X.J. Zhang [a], J. Huang [a], J.P. Qian [a] and X.Z. Gong [a]

[a]*Institute of Plasma Physics, Chinese Academy of Sciences, Hefei 230031, P. R. China*

[b]*University of Science and Technology of China, Hefei, 230026, P. R. China.*

[c]*Advanced Energy Research Center, Shenzhen University, Shenzhen 518060, P. R. China*

[d]*MIT Plasma Science and Fusion Center, Cambridge, MA 02139, USA*

*E-mail: xhd@ipp.ac.cn and bjding@ipp.ac.cn

Abstract

This paper presents the progress in the long - pulse operation of the electron cyclotron (EC) system and the achievements in high - electron temperature plasmas by the combined EC and lower hybrid (LH) waves heating since the EC system was built in 2015. An electron temperature of up to 12 keV with a duration over 100 s was realized by the simultaneous heating of EC and LH waves at the line-averaged density $\bar{n}_e \sim 1.8 \times 10^{19}/\mathrm{m}^3$. The plasma heating effect strongly depends on the location of EC power deposition. H-mode plasmas with solely EC wave auxiliary heating have been obtained on EAST for the first time. These H-mode discharges show an enhanced confinement factor $H_{98(y,2)}$ around 1.0, which is higher than the previous H-mode using LH power alone [*G.S. Xu et al Nucl. Fusion 51 (2011) 072001*]. The total heating power is very close to the threshold value for L-H transition according to the international tokamak scaling. In addition to the temperature effects inside the separatrix, higher electron temperature produced by EC wave is found to reduce the LH power loss in the scrape-off layer (SOL) due to collisional absorption, which is beneficial to further increase the lower hybrid current drive (LHCD) efficiency. Ray-tracing/Fokker-Planck modeling results indicate that higher electron temperature

can shorten the LH wave propagation on EAST in a multiple-pass regime, thus decreasing the collisional dissipation.

1. Introduction

Electron cyclotron resonance heating (ECRH), as an effective core heating tool, has been a well-established approach in tokamak magnetic confinement devices [1-3]. Usually, the EC power is launched as narrow Gaussian beams, which gives rise to highly localized power deposition at the cyclotron resonance layer. Consequently, ECRH and electron cyclotron current drive (ECCD) are recognized to be an effective method for controlling the electron temperature and current profiles in plasmas. An electron temperature (T_e) of up to 26 keV was achieved in JT-60U by injecting EC power of 2.9 MW into the center of a reversed shear plasma produced by the lower hybrid (LH) waves [4]. Unlike other radio frequency (RF) waves, such as LH and ion cyclotron (IC) waves, EC waves can propagate in the vacuum and the coupling is insensitive to the plasma parameters at the edge. As a result, the EC antenna can be placed far away from the plasma boundary, which greatly reduces the risk of damage by plasma–material interactions, especially in a thermonuclear environment. Because of these advantages, a EC system consisting of 20 MW (delivered power) at 170 GHz has been considered on ITER [5] and it was also proposed to be installed on CFETR [6]. On EAST tokamak, which is characterized by steady-state long-pulse operation, the EC system consists of four gyrotron at 140 GHz (corresponding to the magnetic field B_t = 2.5 T for resonance) with total nominal power of 4 MW [7 - 10]. Each of the EC antennas consists of two mirrors with active water cooling, one fixed focusing mirror and one steerable plane mirror. The locations of the steerable plane mirrors are (R, Z) = (3.0 m, -0.3 m) and (3.0 m, 0.3 m) for #1, #2 and #3, #4 gyrotrons, respectively. The launch angles of the steerable mirror can be continuously varied within the range of ≤ 30 ° in the poloidal direction, so that the EC power deposition location can be controlled from the plasma center to the edge. Namely, the poloidal injection angles (α) to the vertical positive direction can be changed from 65 ° to 95 ° for #1 and #2 gyrotrons, as shown in Fig. 1. The toroidal injection angles (β) can be varied between 155 ° - 205 ° for different ECCD requirements. The maximally

allowed angle of 205 ° corresponds to the refractive index parallel to the magnetic field $N_{||} \sim 0.42$ (co-ECCD). EC waves are injected from the lower field side of the torus as an extraordinary mode (X-mode). The cut-off density for the second X-mode EC wave at 140 GHz is as high as $1.9 \times 10^{20}/m^3$ (corresponding to a line-averaged density $\bar{n}_e \sim 1.3 \times 10^{20}/m^3$) according to the CMA diagram, which gives a great margin of operation on EAST ($\bar{n}_e < 6.0 \times 10^{19}/m^3$ in normal operation).

Lower hybrid current drive (LHCD), characterized by the highest CD efficiency with respect to other auxiliary heating and CD methods, has proven to be the main non-inductive method for sustaining long-pulse operation in present tokamaks [11, 12]. Experiments on JT-60 [13], Alcator C-Mod [14], JET [15], Tore-Supra [16] and ASDEX [17] show that the LHCD efficiency was as high as 1 - 3.5 (10^{19} $AW^{-1}m^{-2}$). Here, the LHCD efficiency (η) is defined as

$$\eta = \frac{\bar{n}_e R I_{\mathrm{LH}}}{P_{\mathrm{LH}}} \left(\mathrm{AW^{-1}m^{-2}}\right) \quad (1),$$

where $\bar{n}_e$ is the line-averaged density, R the major radius of the device, I_{LH} the driven current by LH wave and P_{LH} the LH power. LHCD system is also proposed on ITER [18] and CFETR [19] for off-axis current profile control. There are two lower hybrid current drive (LHCD) systems on EAST with different frequencies operating at 2.45 GHz [20] and 4.6 GHz [21]. The 2.45 GHz LH system consists of twenty 200 kW continuous wave (CW) klystrons, and the 4.6 GHz system consists of twenty-four 250 kW CW klystrons. The klystrons were verified to have capability to run at 1000 s on the test bench. The launchers are actively water-cooled for both systems. In 2021, the fully-active-multijunction (FAM) launcher was upgraded to a passive-active-multijunction (PAM) style for 2.45 GHz LH system, while the type of 4.6 GHz launcher is always FAM. Due to the poor heating and CD effects, the 2.45 GHz LH system is rarely used now [22]. Only 4.6 GHz LH is used for the discharges analyzed in this paper.

Both EC and LH systems are the main electron heating and current drive tools in EAST long-pulse operation. With the combination of LH and EC waves, high

performance plasma with β_p ~ 2.0 and $H_{IPB98(y,2)}$ ~ 1.3 has been extended to 60 s (other parameters are: I_p = 350 kA, $\bar{n}_e$ = 4.2 × 10^{19} m^{-3}, residual loop voltage V_{loop} ~ 0 V, energy confinement time τ_E ~ 53 ms) [23], and a super I-mode plasma characterized by both edge transport barriers (ETB) and interal transport barriers (ITB) with a pulse length of 1056 s was achieved recently (other parameters are: I_p = 330 kA, $\bar{n}_e$ = 1.8 × 10^{19} m^{-3}, divertor configuration) [24].

The recent progress in high-electron temperature and long-pulse operation is presented in Section 2. Following this, the H-mode characterization with ECRH as the sole auxiliary heating source is given in Section 3. The temperature effects by ECRH on lower hybrid current drive efficiency are studied in Section 4. Finally, we conclude with a summary in Section 5.

2. Progress in long-pulse and high-electron temperature operation

The first EC system was developed on EAST in 2015 with one gyrotron, and the EC power injected into plasma was at the level of ~ 0.5 MW then. Thanks to the continuous increase in the number of gyrotrons and the improvement of the system, significant progress in high-power and long-pulse operation has been achieved. As shown in Fig. 2, the pulse duration has been extended to ~ 1056 s with P_{EC} ~ 0.55 MW (output by 1 gyrotrons) in 2021, corresponding to the EC energy injected into the plasma ~ 0.58 GJ [24, 25]. High power of 1.6 MW (output by 3 gyrotrons) injected into H-mode plasmas with pulse duration ~ 310 s has been achieved in 2022 [26]. The maximum power coupled into plasmas was ~ 2.0 MW but with short pulse length (~ 10 s). The main factor limiting the power level coupled to plasmas in long-pulse operation (> 100 s) is the overcurrent fault of the gyrotron. The risk of this fault will increase with both the power level and the pulse length. It is worth pointing out that although the EC system consists of four gyrotrons, only three gyrotrons operate in the plasma experiments at the same time. At present, the No. 1 gyrotron is undergoing repair due to the air leakage issue. The main parameters of the high-electron temperature plasmas produced by the combined LH and EC waves are summarized in Table. 1. At the beginning of the system development, the available EC power is only 0.5 MW. As a result, the central electron temperature (T_{e0}) is in the range of 4 – 5 keV

[27]. With the EC power increasing, the T_{e0} increases significantly. When 1.4 MW EC power injecting into the plasma center sustained by 2.4 MW LH wave, the T_{e0} is as high as 12 keV. Figure 3 plots the T_e profiles of these high T_{e0} discharges measured by the Thomson scattering system [28]. The T_e profiles show a steep gradient inside $\rho \sim 0.2$, resulting from the EC power deposition very close to the plasma center, as indicated by the green dotted line. The EC waves are launched perpendicularly (toroidal angle $\beta = 180$ °) and the plasmas are in L-mode with slightly low density for these three discharges. A typical waveform (#98958) of long-pulse and high-electron temperature plasma by the combined LH and on-axis EC heating is illustrated in Fig. 4. The pulse length is over 100 s with line-averaged density $\bar{n}_e \sim 1.8 \times 10^{19}/\mathrm{m}^3$ and loop voltage $V_{loop} \sim 0$. The calculated LH current is peaked at $\rho \sim 0.35$ due to slightly high $N_{||} = 2.26$, consistent with the experimental HXR profile, which helps to optimize the magnetic shear [29].

A direct on-axis heating of EC wave is critical for high-electron temperature production and effective plasma heating, as evidenced by Fig. 5. The increments of the plasma stored energy (W_{MHD}) and of the T_{e0} when the constant EC power is injected into an ohmic plasma are plotted as a function of EC power deposition locations. We changed the EC power location by sweeping the steerable mirror shot by shot. It is seen that when the EC power is deposited close to the plasma periphery ($\rho \sim 0.78$), both the increments of the W_{MHD} and of the T_{e0} are very small ($\Delta W_{MHD} \sim$ 3.0 kJ and $\Delta T_{e0} \sim$ 0.04 keV), while with very central heating ($\rho \sim 0.05$), the incremental central electron temperature ΔT_{e0} reached up to 1.0 keV with the EC power of 0.42 MW. The existence of a helical m/n = 1/1 mode plays a key role in sustaining the high T_{e0} plasmas, as pointed out in [30], where m is the poloidal mode number and n the toroidal mode number. The m/n = 1/1 mode is periodically destabilized by the small-scale turbulence driven by high electron temperature gradient, serving as a sink to release the turbulence free energy, which causes a modulation of the turbulence. This self-regulation system serves as an automatic controller, which dynamically forces the electron temperature gradient in a proper region to sustain the kinetic equilibrium.

3. H-mode characterization

The first H-mode plasmas on EAST were obtained in 2010 with the LH power alone [31]. The confinement enhancement factor $H_{98(y,2)}$ with respect to the so-called IPB98(y,2) scaling [32] was in the range of 0.6 – 1.1. At present, it is easy to get H-mode plasmas during normal operation by the combined LH, EC, ion cyclotron (IC) and (or) neutral beam injection (NBI) heating [23]. However, the H-mode plasmas with ECRH as the sole auxiliary heating source were realized in 2022 for the first time on EAST. The H-mode plasmas using ECRH power alone was firstly observed on DIIID in the 1980s [33], and then reproduced on COMPASS-D [34] and ASDEX Upgrade [35].

Figure 6 displays the time evolution of several key plasma parameters in a typical H-mode discharge (#115676). The plasma current (I_p) is 0.45 MA with an upper single null (USN) divertor configuration and magnetic field on axis B_t = 2.5 T to assure effective plasma heating by EC wave. The EC power was injected during the I_p ramp-up phase with toroidal injection angle of 200 ° (co-ECCD), in order to save the magnetic flux consumption. A favorable B_t direction (namely, $B_t \times \nabla B_t$ towards the primary X-point) and lithium coating were utilized to minimize the threshold power for L-H transition. The L-H transition was triggered at 3.3 s, evidenced by a sharp drop of D_α emission in the divertor chamber, an apparent increase in the plasma stored energy (ΔW_{MHD} ~ 42 kJ) and in the line-averaged electron density, although the gas fueling by supersonic molecular beam injection (SMBI) stopped. After the L-H transition, the discharge entered a quiescent H phase with ELMs free or small ELMs. The H_{89} and $H_{98(y,2)}$ confinement improvement factors with respect to the ITER89-P [36] and IPB98(y,2) [32] scaling laws are about 1.5 and 1.0, respectively, which are 25% and 36% higher than those in L-mode. The total heating power at the L-H transition, $P_{tot} = P_{EC}$ (1.35 MW) + P_{OH} (0.18 MW) is ~ 1.53 MW, which is slightly above the threshold power (~ 1.45 MW) required for an L-H transition according to the scaling law [37]. The T_{e0} measured by electron cyclotron emission (ECE) diagnostic [38] decreases from 2.4 to 2.3 keV after the L-H transition due to the increase in electron density, and the T_{i0} by a toroidal x-ray crystal spectrometer (XCS)

system [39] increases from 0.9 to 1.1 keV as a result of both the electron-ion heat exchange and confinement improvements. In addition, the loop voltage (V_{loop}) drops by ~ 0.11 V, mainly attributed to the significant increase in bootstrap current (I_{BS}) indicated by the poloidal beta β_p ($I_{BS} \propto \beta_p$).

Reliable access to the H-mode has been demonstrated in the range of operational parameters as below: I_p = 0.3 – 0.5 MA, $\bar{n}_e$ = 3.3 – 5.2 (10^{19}/m^3), B_t = 2.5 T, and P_{EC} = 1.1 – 1.8 MW. The $H_{98(y,2)}$ factor for these H-mode discharges is within the range of 0.8 - 1.2, while for the L-mode it is within 0.65 - 0.95, as shown in Fig. 7. It is seen that the energy confinement time is much higher for most data points in L-mode than that in H-mode. This is because the EC power in most L-mode discharges is much lower, namely, P_{EC} = 0.35 – 0.8 MW. Compared with the previous H-mode with LH alone reported in [31], these H-mode discharges show higher confinement. This is because the LH heating effects will become poor at high density, as observed in [40]. With the increase in available ECRH power, the dependence of global confinement on the plasma current, heating power, and plasma density will be investigated in depth in the future.

4. Temperature effects on lower hybrid current drive efficiency

According to the CD theory [41], strong quasi-linear Landau damping will take place when the LH waves reach the region where the thermal velocity $\upsilon_{th} \equiv (kT_e / m_e)^{1/2} \geq 1/3.5\upsilon_{ph}$, where $\upsilon_{ph} \equiv c / N_{||}$, is the parallel (to the background magnetic field) phase velocity of LH waves in the plasmas. This corresponds to the required condition

$$N_{||} \geq \frac{6.5}{\sqrt{T_e\,(\mathrm{keV})}} \qquad (2)$$

for full Landau damping. Consequently, the electron temperature profile has effects on the location of LH power deposition, and also on the velocity of the resonant electrons which is related to the CD efficiency. The effects of ECRH on plasma performance and current profile sustained with LH heating and current drive only were studied in [42, 43] and in [44] previously. In this paper, we focus on the effects of the different T_e profiles produced by ECRH on LHCD efficiency.

4.1 Experimental observations

As given in Section 2, the plasma heating by ECRH strongly depends on the EC power location. Figure 8 shows the time traces of several plasma parameters of two H-mode discharges with different EC power locations. The poloidal (α) and toroidal (β) launch angles for these two discharges are: [α, β] = [77 °, 200 °] (#1 gyrotron, corresponding to ρ_{EC} ~ 0.05) and [α, β] = [103 °, 200 °] (#3 gyrotron, ρ_{EC} ~ 0.05) for #81481; [α, β] = [89 °, 200 °] (#1 gyrotron, ρ_{EC} ~ 0.3) and [α, β] = [85 °, 200 °] (#3 gyrotron, ρ_{EC} ~ 0.5) for #81490. The EC power of the first gyrotron P_{EC1} ~ 0.5 MW and the third gyrotron P_{EC3} ~ 0.55 MW for both discharges. Other parameters, such as the LH power, plasma current (I_p = 400 kA) and density are the same. It is seen that the T_{e0} is as high as ~ 5.4 keV for #81481 with very central heating by EC wave, while for #81490 with outer power depositions, the T_{e0} is only 1.65 keV. The density profiles measured by Thomson scattering system are very similar for both discharges as shown in Fig. 9. The plasma stored energy (W_{MHD}) of #81480 (~ 197 kJ) is higher by a factor of ~ 1.7 than that of #81490 (116 kJ). The hard x-ray (HXR) emission, a proxy for the density of the fast electrons generated by LHCD, is also higher by a factor of ~ 1.72 for #81480, indicating a higher LHCD efficiency. Note that the four sharp increase in HXR signal is due to the neutral beam blips for charge exchange recombination spectroscopy (CXRS) measurements. As plotted in Fig. 10, the HXR profiles, measured by a 20-chord poloidally viewing diagnostic, show a higher intensity and a more peaked shape for #81480. The loop voltage (V_{loop}) is decreased by ~ 0.18 V, suggesting a higher non-inductive current fraction, which consists of LH, EC and bootstrap current. The EC current calculated by TORAY code and the bootstrap current by Sauter model are ~ 35 kA and 175 kA for discharge #81481. Since the V_{loop} is as low as ~ 20 mV, the ohmic current could be ignored. As a result, we get the LH current ~ 190 kA, which is higher by a factor of ~ 5.4 than the EC current. Besides, the internal inductance (l_i) is higher by ~ 0.14, suggesting more plasma current at the core region.

In addition to the above different observations inside the last closed flux surface (LCFS), we also detected two obvious differences in the scrape-off layer (SOL) region. The brightness level detected by a visible camera is much stronger for #81490

(off-axis EC absorption) as compared to #81481 (on-axis EC absorption) on the upper divertor region (USN configurations for these two discharges), the surface of the main limiter and near the LH antenna, as shown in Fig. 11. This result suggests more heat loads on the plasma facing components with lower T_{e0}, as a consequence of more parasitic absorption of LH power in SOL. Secondly, the particle flux measured by Langmuir probe array on upper outer divertor target plate [45] is increased by a factor of ~ 1.4 near the strike point and by a factor of ~ 3 in the private region as shown in Fig. 12. This implies that more LH power are dissipated in the SOL, leading to an enhanced ionization as found in [46].

4.2 Ray – tracing/ Fokker – Planck modeling and analysis

It is well recognized that the LH current will increase with electron temperature and past modelling shows that the LHCD efficiency increases almost linearly with the volume-averaged electron temperature $<T_e>$ before it saturates at much high $<T_e>$ (~ 20 keV) [15, 47]. According to the CD theory [48], the ratio of driven current density J to the LH power density P_D can be expressed as

$$\frac{J}{P_D} = \frac{-e}{m_e \upsilon_{||} \nu} \propto \upsilon_{||}^2 \qquad (3),$$

where ν is the electron-ion collision frequency, and $\upsilon_{||}$ the parallel velocity of the resonant electrons which is $3 - 5\upsilon_{th}$ according to the Landau damping condition shown in equation (2). It was demonstrated in many devices that the LHCD efficiency grew with $<T_e>$, such as in JT-60U [49], JET [15] and FTU [50] experiments. As shown in Fig. 9, the volume-averaged electron temperature is about 1.2 keV and 0.6 keV for #81481 and #81490, respectively. Therefore, it can be concluded that higher electron temperature produced by central EC heating is the first main mechanism responsible for the better LHCD efficiency observed in discharge #81481. In addition, the power loss in SOL due to the collisional dissipation is less, which should be the second reason, as analyzed below.

A combined ray-tracing Fokker-Planck model of GENRAY/CQL3D [51, 52] is utilized to estimate the electron temperature effects on the collisional absorption of LH power in SOL. The wave propagations including in the SOL and the variation in

$N_{||}$ along the propagations are calculated by the ray-tracing code, GENRAY. The electron temperature and density profiles assumed for the simulations are shown in Fig. 9. The launched power spectrum with $2.16 \leq N_{||} \leq 2.36$ is divided into 13 rays and four poloidal launching locations are considered. The same electron density and temperature profiles in SOL are supposed for both discharges as follows: n_e (T_e) = n_{ea} (T_{ea}) × $e^{-r/\lambda}$, where n_{ea} (T_{ea}) = 0.85 × 10^{19}/m^3 (55 eV) is the density (temperature) value at the LCFS, λ = 2 cm (1 cm) the density (temperature) decay length, and r is the distance from the LCFS. Only non-resonant damping due to electron–ion collisions is considered as a loss term.

The calculated ray trajectories in the poloidal plane are shown in Figures 13(a) and (b) for #81480 and #81490, respectively. It is clear that for #81490 with lower T_{e0}, the LH rays undergo much longer propagations in the main plasmas and also in SOL before the LH power is fully absorbed. As a result, the fraction of power loss (P_{cl} / P_{tot}) due to collision in SOL is as high as ~ 39% for #81490, while it is only ~ 6% for #81481 with higher T_{e0}. Figure 14(a) and (b) illustrate the $N_{||}$ pattern (black lines) along the ray trajectories calculated by GENRAY code versus the normalized radius ρ. The red lines represent the strong Landau damping condition as given in expression (2). The blue lines denote the local value of accessibility condition $N_{||}^{acc}$. It is seen that the spectral gap between the $N_{||}$ required for Landau damping (red lines) and the launched $N_{||0}$ = 2.26 is as high as 2.8 for the lower T_{e0} case at the plasma center, while the spectral gap is only 0.54 for #81481 with higher T_{e0}. Landau damping absorption of LH waves does not occur even when the rays penetrate the core region for lower T_{e0} case, and the rays continue to propagate until the upshift of $N_{||}$ becomes large enough induced by the toroidicity effect. The LH current density profiles by CQL3D Fokker-Planck solver are indicated by the yellow lines in Fig. 14. Compared with #81490, there is significant additional LH current in the plasma core for the case of #81481, which is consistent with the experimental measurements of internal inductance (l_i) as shown in Fig. 8. In addition, the calculated line-integrated HXR emission shows a good agreement with the experimental measurements (see Fig. 10). It is worth pointing that in our modeling the synergy effect in the phase space between

LH and EC waves is neglected, which will also increase with the rise of the electron temperature.

In order to investigate the temperature dependence of collisional absorption, a series of simulations is performed with different T_e profiles (shown in Fig. 15), but with the same density profile inside the LCFS and the same density/ temperature profiles in SOL. The calculated results are shown in Fig. 16. It is seen that the power ratio of collisional dissipation to the total power (P_{cl} / P_{tot}) decreases greatly with T_{e0} increasing when T_{e0} is less than 4.0 keV, and the P_{cl} / P_{tot} is less than 10% with T_{e0} increasing to 4.5 keV. On the contrary, the power fraction by electron Landau damping (P_{ELD} / P_{tot}) taking place in the main plasmas increases with T_{e0}. It is worth mentioning that by adding the collisional absorption of LH power in the model, the calculations show dramatically improved agreement with the experiments on Alcator C-Mod [53]. Meanwhile, the numerical calculations with FTU parameters indicate that the parasitic power loss by a collision can be reduced with a hotter plasma edge, thereby increasing the LHCD efficiency [54].

5. Summary

Effective plasma heating effects by EC wave have been demonstrated in EAST long-pulse plasmas. The electron temperature of up to 12 keV with duration over 100 s was achieved by the combined heating of EC and LH waves at the line-averaged density $\bar{n}_e \sim 1.8 \times 10^{19}/m^3$. The pulse length has been extended to 1056 s with moderate EC power ~ 0.55 MW. It is found that the heating effects depend significantly on the EC power deposition location and very central heating is critical for high-electron temperature production. H-mode plasmas with EC wave as the sole auxiliary heating source has been obtained on EAST for the first time. They show better global confinement than the past H-mode using LH power alone. The threshold power for H-mode access is slightly above the value according to the scaling law. Due to the limited available EC heating power, the H-mode scaling of confinement with plasma current, plasma density and heating power has not been investigated in detail.

It is well recognized that higher electron temperature will improve the LHCD efficiency. In our experiments, the measurements by a visible camera and Langmuir

probe array on divertor indicate that higher electron temperature produced by central EC heating is also beneficial to reduce the power loss of LH wave in SOL. Modeling results show that higher electron temperature can shorten the spectral gap between the $N_{||}$ required for Landau damping and the initial $N_{||}$ at the launching point, in the weak damping regime on EAST. Therefore, fewer passes between the plasma edge and center are needed to bridge the spectral gap, leading to less LH power absorption in the SOL by collisional damping. As for ITER [55] and CFETR [56] with much high electron temperatures, most of the LH power will be absorbed in the first single pass. It is foreseen that the effects of collisional damping in the SOL absorption could be ignored.

Additional two gyrotron units are under development, and the total nominal power will be expanded to 6.0 MW. The next plan will focus on the study of H-mode plasmas in wider plasma parameters with more available EC heating power. Besides, the ECCD current will become substantial with the system upgraded. As shown in Fig. 17, the predicted EC current by GENRAY code with L-mode n_e and T_e profiles can be as high as 180 kA with P_{EC} = 2.0 MW, $n_{e0} = 2 \times 10^{19}/m^3$ and T_{e0} = 6.0 keV. In these simulations with parametric scan, the launch angles are fixed and the EC currents are located in a narrow region of $\rho < 0.11$. Hence, the predicted EC currents are expected to mainly depend on the local values ($\rho < 0.11$) of n_e and T_e. The ECCD efficiency and possible synergy effects with LHCD as found on Tore-Supra [57] will be considered in future work.

Acknowledgments

This work was supported by the National Key R&D Program of China (Grant Nos. 2022YFE03010003 and 2017YFE0300401), the National Natural Science Foundation of China (Nos. 11775259, 11975266, 11805233 and 11975276), the Performance Improvement Project of EAST, Hefei Comprehensive National Science Center, Anhui Provincial Natural Science Foundation No. 2008085J04, and the US Department of Energy award DE - SC0010492. The authors would like to thank the experts from GYCOM and CPI companies for their great efforts in the development of gyrotrons

and klystrons for EAST, and to thank Dr J.H. Yang from ASIPP for his valuable comments.

References

[1] Ikeda Y. et al 2002 Nucl. Fusion 42 375.

[2] Parter R. and Petty C. C. 2005 Fusion Sci. and Technol. 48 1141.

[3] Silva M. et al 2011 Fusion Eng. Des. 86 1256.

[4] Suzuki T. et al 2004 Nucl. Fusion 44 699.

[5] Henderson M.A. et al 2008 Nucl. Fusion 48 054013.

[6] Tang Y.Y. et al 2022 Fusion Eng.Des. 182 113225.

[7] Xu H.D. et al 2016 Plasma Sci. Technol. 18 442.

[8] Wang X.J. et al 2015 Fusion Eng. Des. 96-97 181.

[9] Liu F.K. et al 2017 EPJ Web of Conferences 149 01005.

[10] Xu H.D. et al 2021 Fusion Eng. Des. 164 112222.

[11] Houtte D. van et al 2004 Nucl. Fusion 44 L11.

[12] Gong X.Z. et al 2019 Nucl. Fusion 59 086030.

[13] Ushigusa K. et al 2002 Fusion Sci. Technol. 42 255.

[14] Wilson J.R. et al 2009 Nucl. Fusion 49 115015.

[15] Ekedahl A. et al 1998 Nucl. Fusion 38 1397.

[16] Goniche M. et al 2004 Plasma Phys. Control. Fusion 46 899.

[17] Soldner F.X. et al 1994 Nucl. Fusion 34 985.

[18] Hoang G.T. et al 2009 Nucl. Fusion 49 075001.

[19] Liu L. et al 2023 Fusion Eng. Des. 189 113444.

[20] Shan J.F. et al, A New 4 MW LHCD System for EAST, in Proceedings of the 23rd IAEA Fusion Energy Conference, Daejon, Korea (2010).

[21] Liu F.K. et al 2016 Fusion Engineering and Design 113 131.

[22] Li M.H. et al 2016 Phys. Plasmas 23 102512;

[23] Gong X.Z. et al 2022 Nucl. Fusion 62 076009.

[24] Song Y.T. et al 2023 Sci. Adv. 9 eabq5273.

[25] Li M.H. et al *Advance in heating and current drive by RF waves towards long-pulse operation on EAST* the Technical Meeting on Long-Pulse Operation of Fusion Devices Vienna, Austria, IAEA Headquarters, 14–16 Nov. 2022.

[26] Huang J. et al *Progress on Long-pulse Steady-state High Performance Plasmas on EAST* the Technical Meeting on Long-Pulse Operation of Fusion Devices Vienna, Austria, IAEA Headquarters, 14–16 Nov. 2022.

[27] Qian J.P. et al 2016 Plasma Sci. and Technol. 18 457.

[28] Zang Q. et al 2010 Plasma Sci. Technol. 12 144.

[29] Gong X.Z. et al 2022 Plasma Sci. and Technol. (accepted, DOI 10.1088/2058-6272/ac9cc6)

[30] Xu L.Q. et al 2020 Nucl. Fusion 60 106027.

[31] Xu G.S. et al 2011 Nucl. Fusion 51 072001.

[32] ITER Physics Expert Groups on Confinement and Transport and Confinement Modeling and Database 1999 Nucl. Fusion 39 2175.

[33] Lohr J. et al 1988 Phys. Rev. Lett. 60 2630.

[34] Fielding S. J. et al 1998 Plasma Phys. Control. Fusion 40 731.

[35] Sommer F. et al 2012 Nucl. Fusion 52 114018.

[36] Yushmanov P.N. et al 1990 Nucl. Fusion 30 1999.

[37] Doyle E.J. et al 2007 Nucl. Fusion 47 S18.

[38] Liu Y. et al 2016 Plasma Sci. Technol. 18 1148.

[39] Lyu B. et al 2014 Rev. Sci. Instrum. 85 11E406.

[40] Gu X. et al 2018 Phys. Plasmas 25 092509.

[41] Fisch N.J. 1978 Phys. Rev. Lett. 41 873.

[42] Du H.F. et al 2018 Nucl. Fusion 58 066011.

[43] Wu M.Q. et al 2019 Nucl. Fusion 59 106009.

[44] Zhang J.Y. et al 2022 Plasma Sci. Technol. 24 105102.

[45] Xu J.C. et al 2016 Rev. Sci. Instrum. 87 083504.

[46] Petrzilka V. et al 2012 Plasma Phys. Control. Fusion 54 074005.

[47] Takase H. et al 1991 Plasma Phys. Control. Fusion 33 749.

[48] Fisch N.J. 1987 Rev. Mod. Phys. 59 175.

[49] Ushigusa K. et al 1989 Nucl. Fusion 29 1052.

[50] Pericoli-Ridolfini V. et al 2005 Nucl. Fusion 45 1386.

[51] Smirnov A.P. and Harvey R. 1995 Bull. Am. Phys. Soc. 40 1837.

[52] Harvey R.W. and McCoy M. in Proceedings of the IAEA Technical Committee Meeting on Simulation and Modeling of Thermonuclear Plasmas, Montreal, 1992, International Atomic Energy Agency, Vienna, 1992, pp. 489-526.

[53] Wallace G.M. et al 2010 Phys. Plasmas 17 082508.

[54] Barbato E. 2011 Nucl. Fusion 51 103032.

[55] Decker J. et al 2011 Nucl. Fusion 51 073025.

[56] Wallace G.M. et al 2021 Nucl. Fusion 61 106009.

[57] Giruzzi G. et al 2004 Phys. Rev. Lett. 93 255002.

Captions

Table 1 Main parameters of the high – electron temperature plasmas by the combined LH and EC waves

Shot No.	Ip (MA)	$\bar{n}_e$ (10^{19}/m^3)	V_{loop} (mV)	P_{EC} (MW)	P_{LH} (MW)	T_{e0} (keV)	Gyrotrons
#59585	400	1.55	0	0.5	1.8	4.2	1
#78841	450	1.8	-20	0.9	1.8	9.0	2
#98958	500	1.7	-29	1.4	2.3	12.0	3

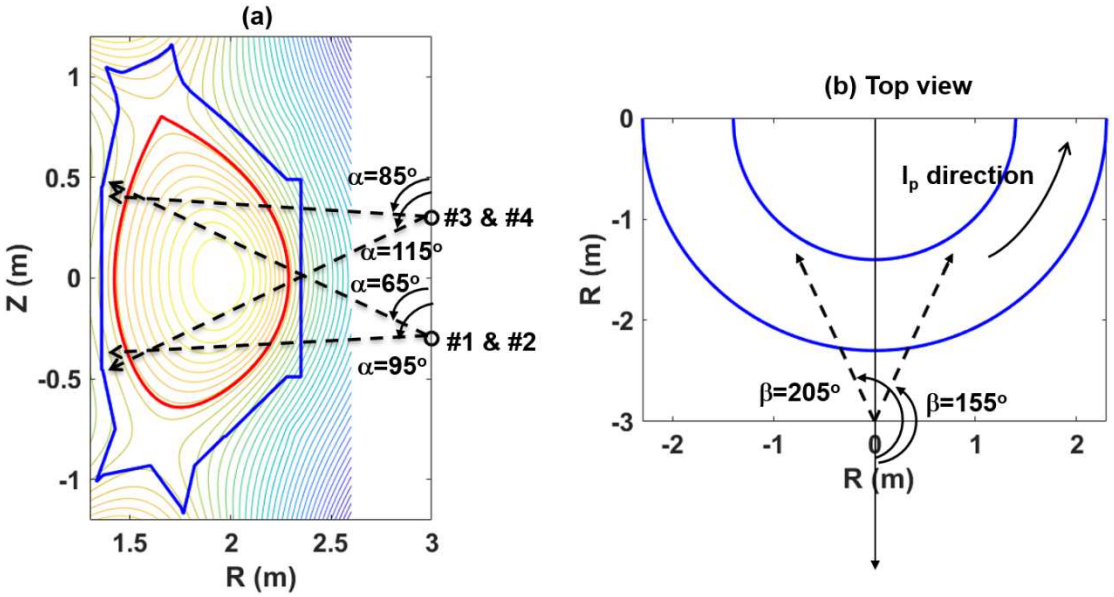

Fig. 1 Definition of the poloidal injection angle (a) and toroidal angle (b) of EC waves. The locations of the steerable mirrors denoted by the black circles are (R, Z) = (3.0 m, -0.3 m) and (3.0 m, 0.3 m) for #1, #2 and #3, #4 gyrotrons, respectively. The poloidal angles can be continuously varied within the range of ≤ 30 °, namely, from 65 ° to 95 ° for #1, #2 gyrotrons, and from 85 ° to 115 ° for #3, #4 gyrotrons. The toroidal injection angles can be varied between 155 ° - 205 °. The EC wave injected with β = 180 ° corresponds to only plasma heating and the one with β > 180 ° corresponds to co-ECCD.

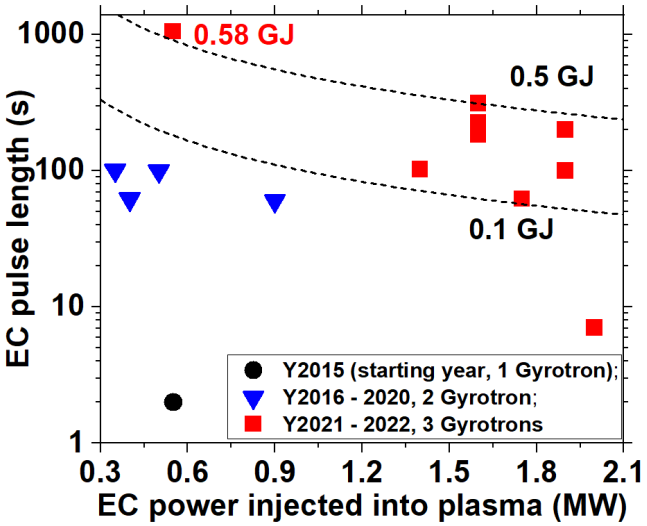

Fig. 2 Progress in the EC power injected into plasma and in its pulse duration on EAST.

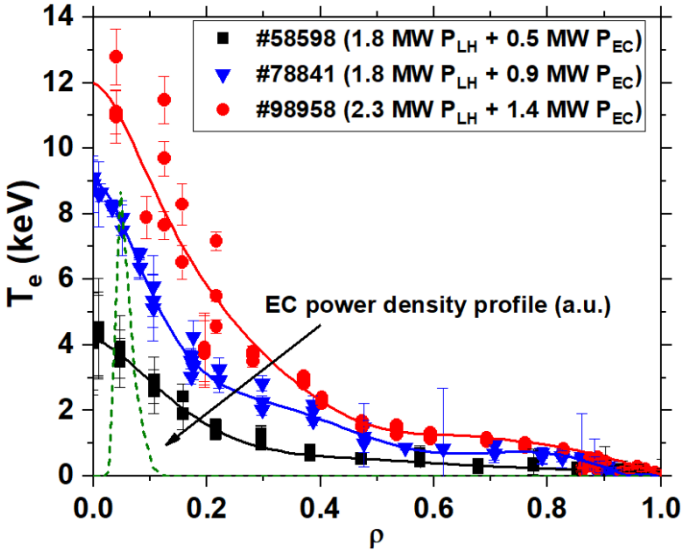

Fig. 3 Electron temperature (T_e) profiles measured by Thomson scattering. The calculated EC power deposition profile is indicated by green dotted line. The three discharges are in L-mode.

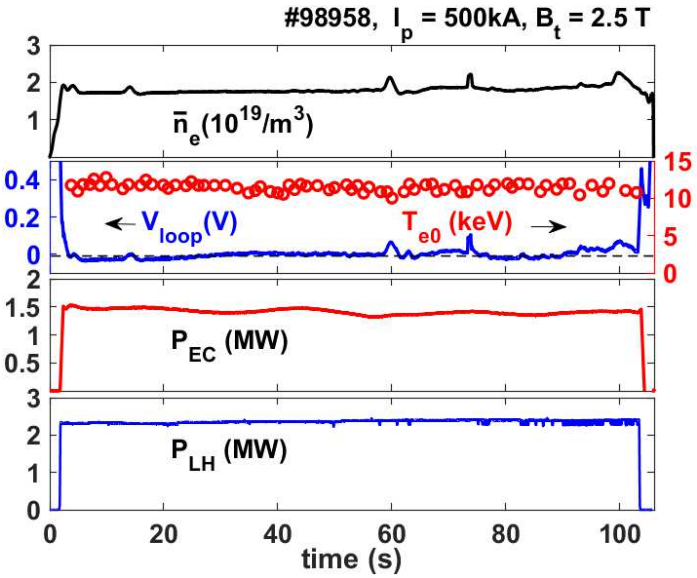

Fig. 4 Typical L-mode waveform of a long-pulse and high – electron temperature plasma by the combined LH and on-axis EC heating. I_p plasma current, B_t magnetic field on axis; $\bar{n}_e$ line-averaged density; V_{loop} loop voltage; T_{e0} electron temperature at plasma center; P_{EC} and P_{LH} EC and LH power.

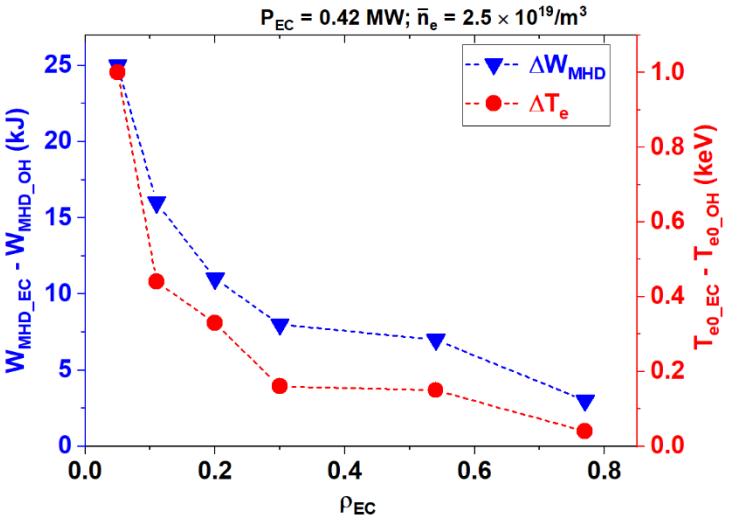

Fig. 5 The increment of plasma stored energy (W_{mhd}) and central electron temperature (T_{e0}) after EC power injected into ohmic plasmas versus EC power deposition locations. All the discharges are in L-mode and the EC wave is injected perpendicularly ($\beta = 180$ °).

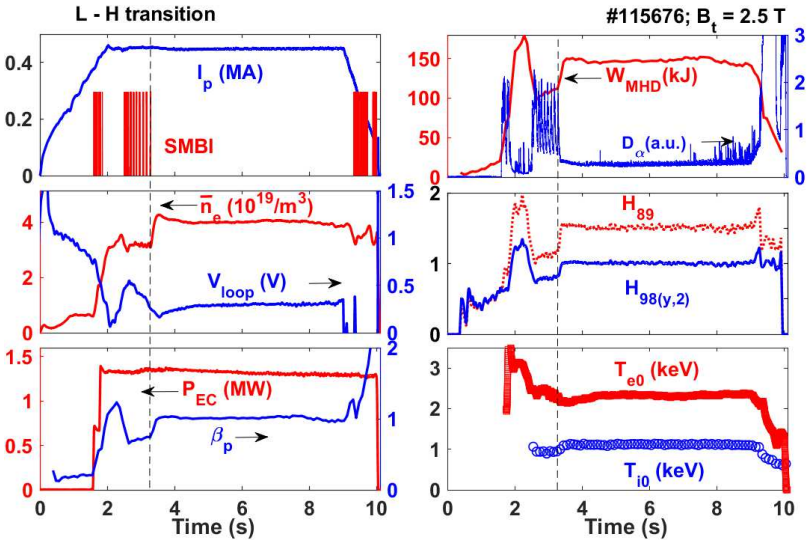

Fig. 6 Time evolution of several key plasma parameters in a typical H-mode discharge with solely EC wave auxiliary heating. SMBI supersonic molecular beam injection; D_α deuterium emission in the divertor; H_{89} and $H_{98(y,2)}$ confinement improvement factors with respect to the ITER89-P and IPB98(y,2) scaling laws; β_p poloidal beta. The L-H transition occurred at t = 3.3 s.

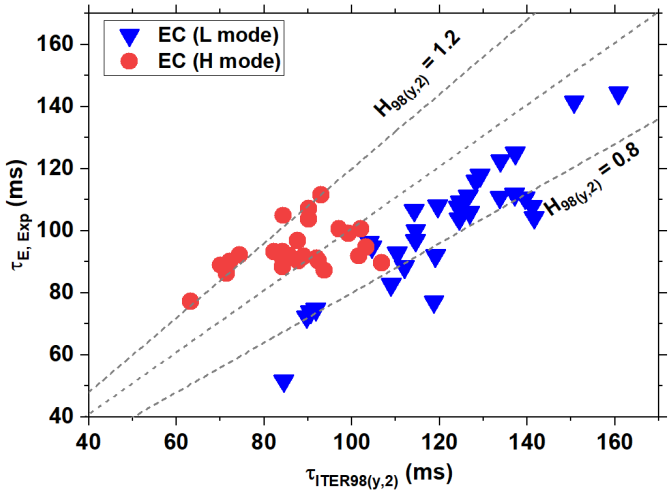

Fig. 7 Experimental confinement time versus the IPB98(y,2) scaling law for L and H-mode plasmas with solely EC wave auxiliary heating.

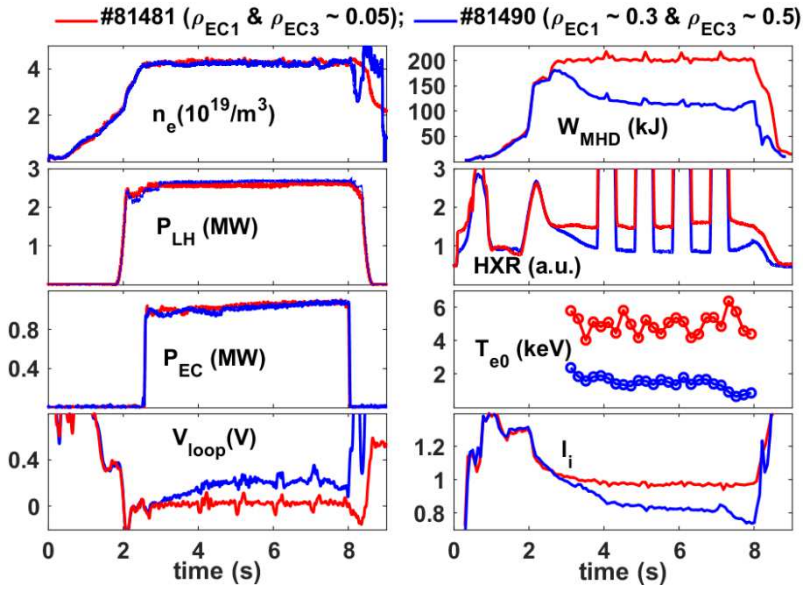

Fig. 8 Time traces of several plasma parameters of two H-mode discharges with different EC power locations. HXR hard x-ray emission; l_i internal inductance; ρ_{EC} the normalized radius at the peak of the EC power deposition profile. The EC power of the first gyrotron P_{EC1} ~ 0.5 MW and the third gyrotron P_{EC3} ~ 0.55 MW for both discharges. The four jumps of HXR signal are due to the neutral beam blips for charge exchange recombination spectroscopy (CXRS) measurements. The plasma current I_p = 400 kA for both discharges.

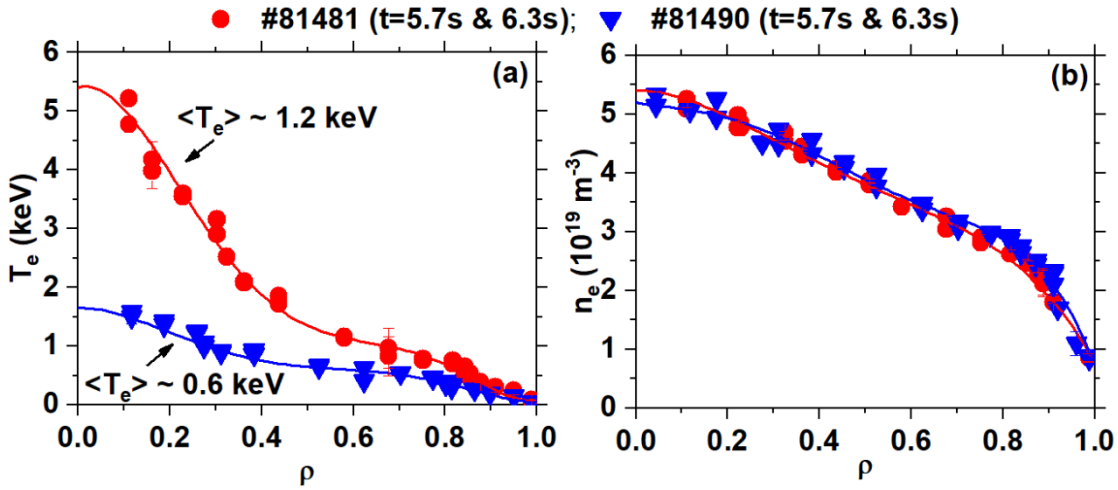

Fig. 9 Electron temperature (a) and density (b) profiles measured by Thomson scattering for #81481 with ρ_{EC1} & ρ_{EC3} ~ 0.05, and for #81490 with ρ_{EC1} ~ 0.3 & ρ_{EC3} ~ 0.5.

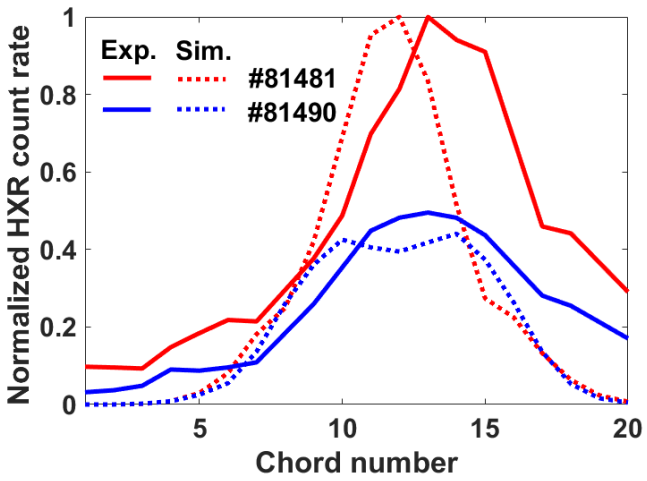

Fig. 10 Experimental and simulated HXR count rate profiles. Both experimental and simulated profiles are normalized by the maximum value.

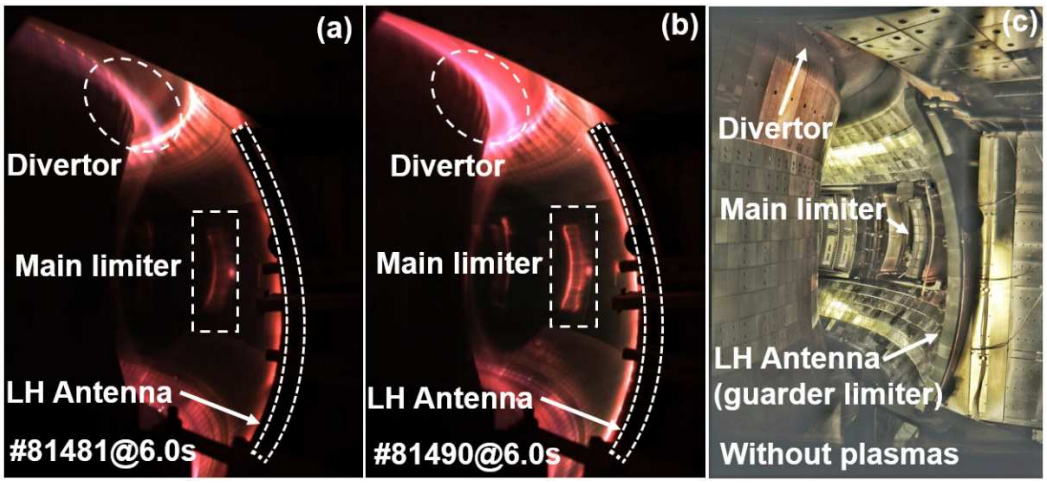

Fig. 11 Images from a visible camera. The main limiter of EAST and the LH antenna are also shown. The third picture was taken without plasma to show the internal components more clearly.

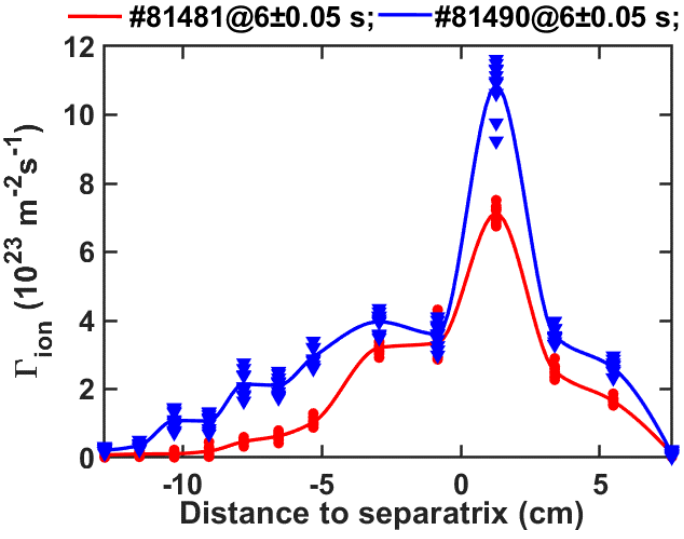

Fig. 12 Particle flux profiles measured by Langmuir probe array on the upper outer divertor target plate.

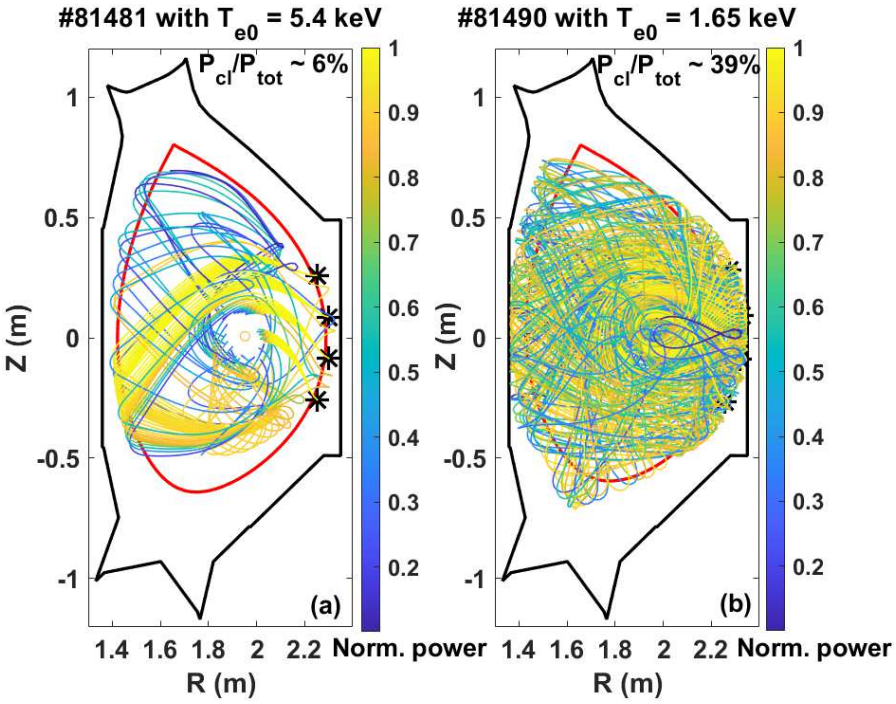

Fig. 13 Ray trajectories in the poloidal plane calculated with the GENRAY code, including propagation in the SOL region for #81481 with higher T_{e0} (a) and for #81490 with lower T_{e0} (b). The color bar denotes the normalized ray power to the initial power. The thick red curve indicates the last closed flux surface, and the four black asterisks at the low field side represent the poloidal launching locations. The power ratio of the collisional damping to the total power is indicated for both discharges.

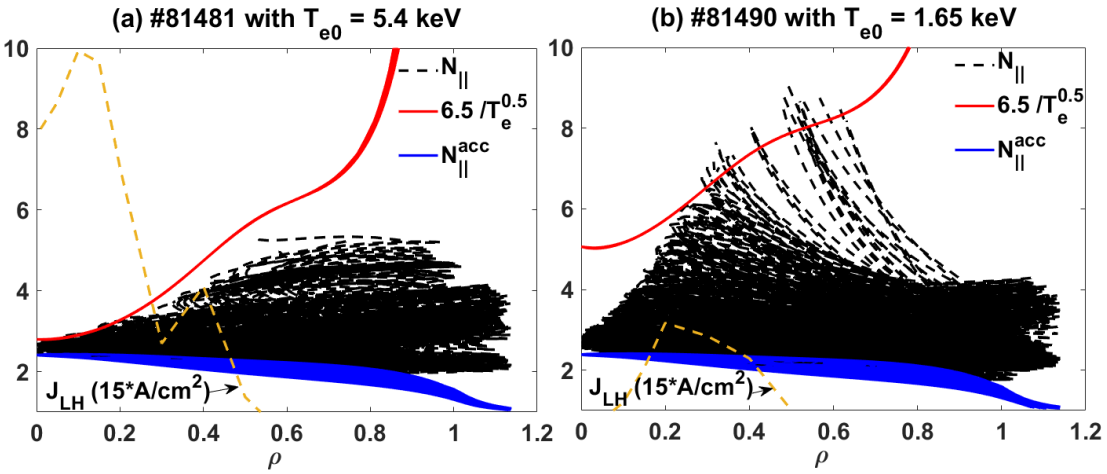

Fig. 14 $N_{||}$ pattern (black lines) along the ray trajectories calculated by GENRAY code versus the normalized radius ρ. The red lines represent the strong Landau damping condition. The blue lines denote the local value of $N_{||}^{acc}$. $N_{||0}$ = 2.26 at the launching point. The LH current density profiles indicated by the yellow lines are predicted by CQL3D.

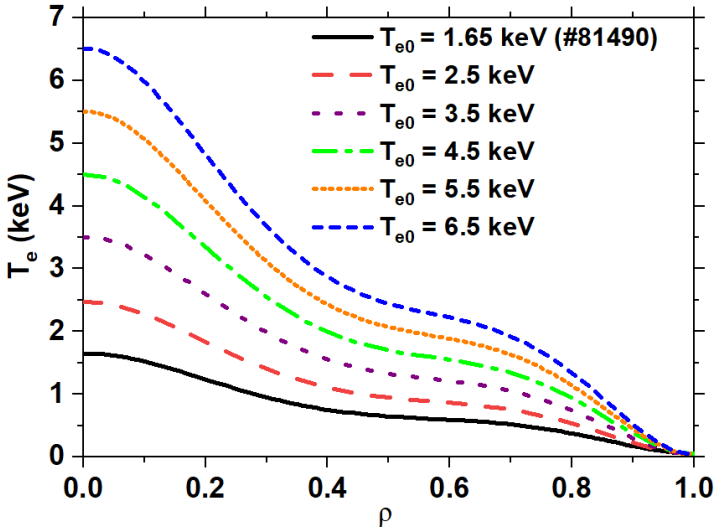

Fig. 15 Assumed electron temperature profiles with different T_{e0}, which are scaled up with the experimental profile of #81490 (black line).

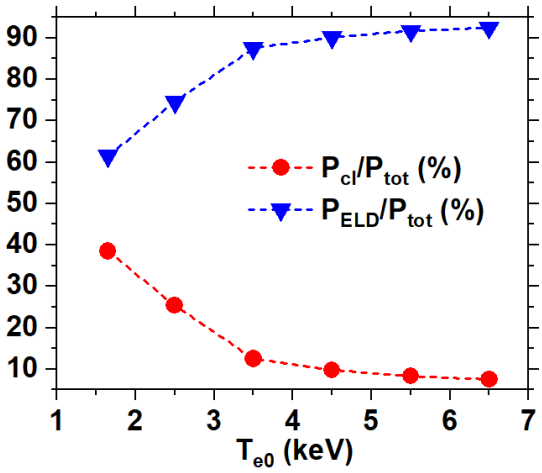

Fig. 16 Power ratio of collisional dissipation and electron Landau damping to the total power as a function of T_{e0}, calculated with different T_e profiles as shown in Fig. 14. The density profile inside the LCFS and the density/ temperature profiles in SOL are kept unchanged. The launched $N_{||0}$ = 2.26.

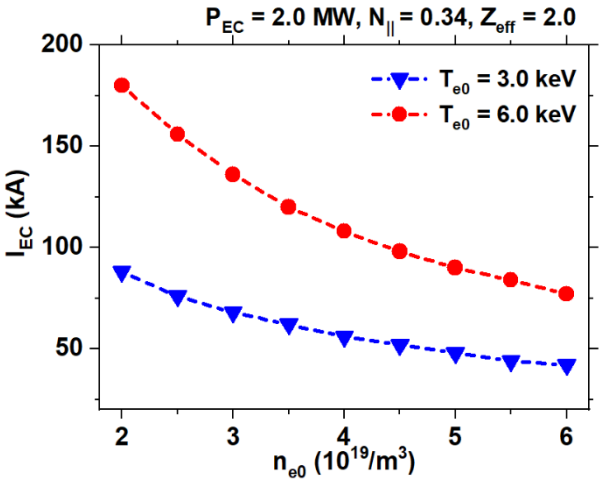

Fig. 17 EC current predicted by TORAY code as a function of central electron density with P_{EC} = 2.0 MW, $N_{||}$ = 0.34 and the effective charge number Z_{eff} = 2.0. Two cases with different T_{e0} are considered. The density and temperature profiles assumed for the prediction are $n_e = (n_{e0} - n_{ea}) \times (1 - \rho^2)^2 + n_{ea}$ and $T_e = (T_{e0} - T_{ea}) \times (1 - \rho^2)^2 + T_{ea}$, where n_{ea} and T_{ea} are the density and temperature at $\rho = 1$.